Benzothiazole-Derived Covalent Organic Framework for Multimedia Iodine Uptake

Ritika Jaryal
Dr. B. R. Ambedkar National Institute of Technology Jalandhar
Sadhika Khullar
Dr. B. R. Ambedkar National Institute of Technology Jalandhar
Rakesh Kumar (rakeshkumar@nitj.ac.in)
Dr. B. R. Ambedkar National Institute of Technology Jalandhar

Research Article

Keywords: Covalent organic frameworks (COFs), Benzothiazole, Phenylenediamine, β-ketoenamine, Iodine adsorption, Iodine release

Posted Date: June 30th, 2023

DOI: https://doi.org/10.21203/rs.3.rs-3100667/v1

Abstract

Nuclear energy holds the chief portion of the global primary energy mix that comes with the major issue of releasing volatile nuclear wastes *viz.* radioiodine (^{129}I and ^{131}I) into air and water bodies during nuclear fuel reprocessing. The efficient capture of volatile radioiodine has attracted a major attention worldwide due to the severe health and environment effects. Among various porous materials, covalent organic frameworks (COFs) are the intriguing class of porous organic materials with crystallinity, synthetically pre-designable functionalities to achieve tunable properties. Herein, a new benzothiazole based COF (COF-3) obtained by the condensation of 2,6-dimainobenzothiazole and 2,4,6-triformylpholoroglucinol is reported with tetragonal pore topology (pore volume = 0.305 cc/g; BET surface area = 57.9 m^2/g). The electron rich heteroatoms in the frameworks play a crucial role in adsorbing electron deficient iodine molecules and therefore, the benzothiazole-derived COF is envisioned to be potent material for efficient iodine adsorption. The synthesized COF showed the iodine adsorption capacity of 1.07 g g^{-1} in vapor phase and 109.0 mg g^{-1} from *n*-hexane solution. A reference COF (COF-4) with no thiazole group derived from 1,4-phenylenediamine and 2,4,6-triformylpholoroglucinol with hexagonal pore topology (pore volume = 0.937 cc/g) and BET surface area 133.9 m^2/g showed adsorption of iodine from *n*-hexane solution with capacity 149.5 mg g^{-1}. The study revealed that although the presence of heteroatoms in the framework facilitates the iodine adsorption by converting the molecular iodine into the polyiodides; the factors such as BET surface area, pore topology and pore volume also play a major role in the adsorption of iodine molecules.

Introduction

Nuclear energy is a sustainable, low carbon and economically competitive energy with a potential to share the major chunk of the future global energy consumption. According to British Petroleum (BP) Statistical Review of World Energy 2021 (70th edition), nuclear energy holds 4.3% share of the global primary energy mix [1]. 2021 witnessed the largest rise in nuclear energy generation (4.2%) since 2004 led by China [2]. However, the safety related issues associated with the operations of the nuclear power plants, improper disposal of the generated radioactive waste and the risks of nuclear accidents outweigh the several advantages of the nuclear energy. Various radioactive iodine isotopes, majorly Iodine-129 (^{129}I) and Iodine-131 (^{131}I) are released into the gas streams and aqueous solutions during nuclear fuel treatment. ^{131}I has the high radioactivity (half-life, $t_{1/2}$ = 8.04 d) and is potentially active to incorporate into the human metabolic process through bioaccumulation in food chain. On the other hand, ^{129}I has a very long life time ($t_{1/2}$ = 1.6 × 10^7 y) and the isotope poses a greater disposal risk [3, 4]. Indeed, the studies revealed that radioiodine was the major contributor to the thyroid cancer caused by Chernobyl and Fukushima nuclear disasters in 1986 and 2011, respectively [5, 6]. Thus, an effective capture of radioiodine during the nuclear disasters as well as routine waste treatment is a major global concern.

The typical nuclear fuel reprocessing conditions involve ambient pressure and 77°C temperature under which the iodine exists as a coagulative vapor. In this context, various removal techniques for the

coagulative radioiodine vapors have been exploited. However, the adsorption based removal techniques are considered better over traditional liquid scrubbing processes because of the low maintenance cost, easy operation and non-usage of corrosive solutions [7]. These adsorption based processes are effectively strategized by using (1) silver based adsorbent to convert iodine to silver iodide [8–10]; (2) adsorbents containing frameworks with electron rich heteroatoms sulfur (S), nitrogen (N) and oxygen (O) as well as the π-donors such as aromatic ring, double/triple bonds or conjugated systems to adsorb electron deficient iodine leading to the formation of charge transfer complexes[11–16]; (3) functionalizing the adsorbents with ionic groups such as $[RN\text{-}(CH_3)_3]^+ \cdot X^-$ to adsorb iodine *via* the coulombic interactions [17]. The silver based adsorbents render less efficiency due to a low stoichiometrically maximum adsorption capacity of 1.18 g per gram of Ag and with lesser practical capacities of the order of 0.10–0.31 g g^{-1}.[10] The high cost of silver also renders these materials ineffective for commercial use.

Based on the adsorption mechanisms, various materials such as ceramics [18, 19], aerogels [20, 21], metals such as silver [22], conjugated polymers [23, 24], zeolites [25–30], metal organic frameworks (MOFs) [31–37] *etc.* have been explored as the potential adsorbents till now for the capture of radioiodine. Covalent organic frameworks (COFs) are the emerging organic polymers with fascinating properties such as highly ordered and crystalline structures, excellent stability, large surface areas and permanent porosity [38–43]. Further, several advantages such as the structural predesignability, synthetic flexibility and post-synthetic functional group modifications are amenable to tune the properties of these frameworks to achieve materials with low densities and high efficiencies. In recent years, COFs have been explored as impressive adsorbent materials with a broad scope in several applications such as gas adsorption and storage, catalysis, semiconductors and photoconducting devices [13–14, 44–49]. Suitably designed heteroatom containing electron rich COFs are envisioned as potent materials in adsorbing electron deficient iodine [50–56]. Zhao *et al*. showed the iodine adsorption capability of COFs in both the vapor state and in the solution. They found that the abundance of aromatic rings were advantageous for iodine adsorption, high nitrogen content, and well-ordered network [47]. The adsorption of iodine within the cavities of the COFs involve the physical adsorption that depend upon the pore volume, pore topology, pore size and the BET surface area of the frameworks. Then, interaction of electron density of the frameworks with electron deficient iodine molecules which may or may not convert them into polyiodides depending upon the type of connectivity, type of electron rich heteroatoms or functionalities occurs. These polyiodides further, help in adsorbing more iodine molecules through chemical adsorption [48]. A recent study showed that Schiff base linkage in the COFs plays an important role in the iodine adsorption capacity [57]. The imine-linked COF showed excellent iodine adsorption both in vapor phase (5.82 g g^{-1}) as well as from the solution of iodine in *n*-hexane (99.9 mg g^{-1}). The higher adsorption in these COFs was attributed to the polarity of the C = N bond, a Lewis structure to bind iodine according to the charge transfer (CT) theory. The oxidizing components of the COF structure have the tendency to convert partially or completely iodine into polyiodides. These adsorbents and polyiodides have the strong interaction to bind iodine molecules within the frameworks. COFs based on imine linkages also possess excellent thermal stability and chemical resistant properties [58].

Intrigued by the recent studies, COFs with heteroatom containing molecular scaffolds were desired. Benzothiazole moiety comprising of a significant π-character and *N* and *S* heteroatoms could provide an effective template for the physisorption through van der Waals interactions as well as the chemisorption of iodine through the formation of polyiodides. In the current study, synthesis and iodine adsorption ability of a benzothiazole-derived, β-ketoenamine linked COF (COF-3) is reported. The iodine adsorption capacity of the new COF is also compared with the previously reported TpPa-1 (COF-4).

Materials and Methods

Chemicals

1,4-phenylene diamine, phloroglucinol, 2-amino-6-nitrobenzothiazole, phosphorus oxychloride ($POCl_3$), trifluoroacetic acid (TFA), hydrochloric acid (HCl), hexamethylenetetramine (HMTA), N,N-dimethylformamide (DMF), mesitylene, 1,4-dioxane, acetone, tetrahydrofuran (THF), methanol were purchased from Avra. All the chemical reagents were of analytical grade and used without further purification.

Methods

Synthesis of 2,4-diformylphloroglucinol (1).

In a 10 mL round bottom flask containing 0.7 mL dimethylformamide (DMF) and 0.8 mL phosphoryl chloride ($POCl_3$) were added dropwise under nitrogen atmosphere and reaction mixture was allowed to stir for 45 minutes. In another 10 mL round bottom flask, 500 mg phloroglucinol was added into 3.5 mL dioxane. To this, DMF/$POCl_3$ solution was added dropwise with continuous stirring under nitrogen atmosphere and allowed to stir for 12 hours. An off-white amorphous solid was formed that was transferred to another round bottom flask containing ice and further, allowed to stir for 4 hours. The off-white precipitates were filtered and washed with cold water. The obtained precipitates were refluxed in water for 15 minutes resulted into salmon orange-colored precipitates that were filtered, washed with excess of water and dried to afford 450 mg (65%).^{1}H NMR (DMSO-d_6, 500 MHz, ppm) 12.49 (Broad s, 3H), 10.01 (s, 2H), 5.90 (s, 1H) [59] (Fig. S1).

Synthesis of 2,4,6-triformylphloroglucinol (2).

In a 10 mL round bottom flask, 250 mg of 2,4-diformylphloroglucinol and hexamethylenetetramine (HMTA) (288 mg, 2.05 mmol) were dissolved in 2 mL trifluoroacetic acid (TFA). The reaction mixture was refluxed for three hours. Then, 7 mL 2M HCl solution was added to the solution and refluxed for one hour. Light red-coloured precipitates were filtered and washed with water to afford 210 mg (73%). ^{1}H NMR (DMSO-d_6, 500 MHz, ppm): 9.99 (s, 3H), 5.89 (s, 3H) [59] (Fig. S2)

Synthesis of 2,6-diaminobenzothiazole (3).

2.0 g (10.25 mmol) of 2-amino-6-nitrobenzothizole was dissolved in ethanol (80 mL) in a 250 mL two-neck round bottom flask. A solution of $SnCl_2.2H_2O$ (16.14 g, 71.7 mmol) in ethanol (20 mL) was added to the reaction mixture that was allowed to stir at 70°C for 24 h. The resulting milky white colored suspension was poured in ice cold water and neutralized with Na_2CO_3 until the pH of the mixture reached 7.0. The desired product was obtained by filtration of the reaction mixture with ethyl acetate as an organic solvent. The ethyl acetate layer containing the product was evaporated under reduced pressure to give light brown coloured powder with yield of 1.62 g (95.6%). ^{1}H NMR (DMSO-d_6, 500 MHz, ppm): 7.02 (d, 1H, J = 8.4 Hz), 6.91 (s, 2H), 6.81 (d, 2H, J = 2.2 Hz), 6.49 (dd, 1H, J_1 = 8.5, J_2 = 2.3 Hz), 4.82 (Broad s, 2H).

Synthesis of COF-3

An Erlenmeyer flask was charged with 1,3,5-triformylphloroglucinol (63 mg, 0.3 mmol), 2,6-diaminobenzothiazole (89 mg, 0.54 mmol), 5 mL of (1:1) mesitylene: dioxane and the mixture was homogenized by sonication for 10 minutes. 6 M AcOH (2.0 mL) was added to the obtained orange suspension after sonication and then transferred to reactor. The mixture was heated for 3 days at 120°C. Dark brown precipitates were filtered and washed with *N,N*-dimethyl formamide, DCM, methanol and THF, respectively. The washed precipitated were dried in an oven for 24 h at 70°C to afford 120 mg of red-brown powder.

Synthesis of COF-4

An Erlenmeyer flask was charged with 1,3,5-triformylphloroglucinol (140 mg, 0.67 mmol), *p*-phenylenediamine (130 mg, 1.2 mmol), 5 mL of (1:1) mesitylene: dioxane and the mixture was homogenized by sonication for 10 minutes. 6M AcOH (2.0 mL) was added to the obtained orange suspension after sonication and then transferred to reactor. The mixture was heated for 3 days at 120°C. Dark brown precipitates were filtered and washed with *N,N*-dimethyl formamide, DCM, methanol and THF, respectively. The washed precipitates were dried in an oven for 24 h at 70°C to afford 217 mg of red-brown powder.

Vapour Phase Iodine Adsorption

The capture of volatile iodine was studied by simulating nuclear fuel reprocessing conditions. BT-COF (40 mg) was placed in a guard tube whose one mouth was fitted to a round bottom flask containing solid iodine and other mouth was closed to avoid air contamination. Vaporized iodine was obtained by heating solid iodine at 77 ˚C under ambient pressure conditions. After the adsorption of iodine vapours for a period of time, the weight of iodine capture COF was taken at room temperature. The uptake ability of COF for iodine was calculated using the Eq. (1):

$$\mathrm{C_e} = \frac{(\mathrm{W_i} - \mathrm{W_t})}{\mathrm{W_i}} \mathrm{x100wt\%}$$

1

Where, C_e is the iodine uptake capacity, W_i and W_t are the weights of COF before and after the iodine capture [54].

Liquid Phase Iodine Adsorption-Desorption

Iodine Adsorption

5 mg of COF was added to 5 mL of iodine/*n*-hexane solution at various concentrations of 50, 100, 150, 200 mg L^{-1} at 30°C with stirring for a period of 4.5 hours. The residual iodine readings were taken at various time intervals using UV–Vis spectrophotometer at 522 nm. The iodine adsorption quantity (q_t; mg g^{-1}) and the removal efficiency (ω %) were calculated using Eqs. (2) and (3).

$$q_t = (C_o - C_t)\, x \frac{V}{W}$$

2

$$\omega\% = \frac{(C_o - C_t)}{C_o} x100 \quad (3)$$

Where, C_o and C_t are the initial and final concentrations of iodine/*n*-hexane solution (mg L^{-1}), V is the volume of iodine/*n*-hexane solution taken (L) and W is the weight of the COF taken (g) [54].

Kinetics analysis and adsorption isotherms:

The adsorption kinetics of iodine/*n*-hexane solution was analyzed using pseudo-first-order and pseudo-second-order kinetic models using equations (4) and (5).

$$\ln (q_e - q_t) = \ln q_e - K_1 t$$

4

$$\frac{t}{q_t} = \frac{t}{q_e} + \frac{1}{K_2 q_e^2}$$

5

Where, q_e (mg g^{-1}) and q_t (mg g^{-1}) are the iodine adsorption quantities at equilibrium and time t (min), respectively. K_1 (min^{-1}) and K_2 (min^{-1}) are the rate constants for pseudo-first-order and pseudo-second-order adsorptions, respectively.

Adsorption isotherm was analyzed using Langmuir and Freundlich isotherm models according to the equations (6) and (7):

$$\frac{1}{q_e} = \frac{1}{q_e K_L C_e} + \frac{1}{q_m}$$

6

$$\ln q_e = \ln K_F + \frac{1}{n} \ln C_e$$

7

Where, q_e (mg g^{-1}) and q_m (mg g^{-1}) represent the iodine adsorption quantities at equilibrium and maximum adsorption capacity, respectively. C_e (mg L^{-1}) is the concentration of iodine at equilibrium. K_L signifies the Langmuir equilibrium adsorption constant, K_F signifies the Freundlich constant and 1/n represents the adsorption intensity (mg L^{-1}) [54].

Iodine Desorption

Trapped iodine was released by immersing iodine loaded COFs in methanol at 30°C. 5 mg of I_2@COF was immersed in 5 mL of methanol solution and the releasing process was studied at various time slots *via* UV–Vis spectrophotometer at 290 and 359 nm.

Characterizations

The structure of COF was characterized by using ATR-IR BUKER ALPHA II, Germany in a range of 4000 – 400 cm^{-1} and solid-state ^{13}C NMR analysis using ECZR Series 600 MHz NMR Spectrometer with 20 KHz spinning speed and variable temperature range between − 20°C to + 80°C. The crystallinity of the COF was determined by using PXRD analysis and diffraction patterns were recorded in a 2θ range of 5–60° on RIGAKU using Cu–Kα radiation (l.14, 1.54) at a scan rate of 3 min^{-1}. Structural modelling, theoretical PXRD pattern calculations, Pawley refinement were carried out using Materials Studio software package. The geometrical optimizations were done using Forcite tool. Then, Pawley refinement was done using Reflex tool. The morphology and size of the COF was determined using FE-SEM (CARL ZEISS GEMINI 1 SIGMA 500 VP) and HR-TEM with charge couple device (CCD) coupled device within the working voltage range of 80 to 200 kV. Thermal stability of the COF was studied by SII EXSTAR 6000 TGA thermal analyzer at a heating rate of 10°C/min within temperature range of 30°-600°C. The adsorption/desorption isotherm and pore volume of the COF was determined by nitrogen adsorption-desorption isotherm measured at 77 K using Quanta chrome Autosorb 1C system. The BET surface area and pore properties were determined by calculation from the adsorption branch. The chemical composition of the framework was characterized using X-ray photoelectron spectroscopy which was conducted at room temperature using a Nexsa (ThermoFisher Scientific) instrument with an Al Kα X-ray source. The UV-Vis spectra were recorded using an Agilent Cary-5000 UV-Vis-NIR spectrophotometer.

Results and Discussion

Structure and composition

β-Ketoenamine-linked COF-3 and COF-4 were synthesized *via* the solvothermal condensation of 2,6-diaminobenzothiazole,1,4-phenylenediamine, respectively with 2,4,6-triformylphloroglucinol as depicted in Scheme 1. The synthesized COFs were characterized using ATR-Infra-red (IR), solid-state NMR spectroscopy, powder X-ray diffraction (PXRD), FE-Scanning Electron Microscopy (FE-SEM), high resolution Transmission Electron Microscopy (HR-TEM), X-ray Photoelectron Spectroscopy (XPS) and Thermogravimetric analysis (TGA).

IR spectra of the two COFs revealed the disappearance of characteristic bands of the starting materials *i.e.* N-H stretching (3100–3400 cm^{-1}) and aldehyde carbonyl stretching (1645 cm^{-1}) bands, that confirmed the complete Schiff base condensation reaction between the monomers (Figs. 1 & 2) [60]. Both the COFs showed *β*-ketoenamine linkage in their structures as evident from the absence of O-H stretching and C = N stretching bands, the characteristic bands for the structure to exist in the enol form. The tautomerism between the *β*-positioned hydroxyl groups and Schiff bonds (C = N) leads to the intramolecular NH-O hydrogen bonding resulting into the *β*-ketoenamine linkages. Also, the appearance of C-N stretching peaks at 1262 cm^{-1} and 1259 cm^{-1}, the characteristic peak of *β*-ketoenamine linkage in case of COF-3 and COF-4, respectively was also observed. No C = O stretching band corresponding to keto group of the framework was observed in the IR-spectra of both the COFs. This is because C = O stretching band merged with the C = C stretching band at 1588 cm^{-1} and 1582 cm^{-1} in the extended structures both the COFs *viz.* COF-3 and COF-4, respectively.

The atomic-level construction of both the COFs was further verified by ^{13}C cross-polarization magic angle-spinning (CP-MAS) solid-state carbon NMR spectroscopy. NMR spectrum of COF-3 showed the signals at 185.80 ppm corresponding to carbonyl group of the *β*-ketoenamine linkage in the framework (Fig. S4). The signals at 148.53 ppm, 133.19 ppm, 121.42 ppm and 106.28 ppm correspond to aromatic carbons. The signals at 171.19 ppm and 161.35 ppm were attributed to the presence of thiazole in the structure of COF-3. Also, COF-4 showed signals at 106.32 ppm, 115.04 ppm, 121.85 ppm, 135.69 ppm and 183.78 ppm corresponding to aromatic carbons and carbonyl group of *β*-ketoenamine linkage, respectively (Fig. S5).

The powder X-ray diffraction patterns of the synthesized COFs showed their semi-crystalline nature. COF-3 displayed diffraction peak at 26.28° corresponding to the (002) reflection plane and COF-4 exhibited the major diffraction peak at 26.12° corresponding to the reflection from (201) plane. The π − π stacking distances between the COF-3 layers was 3.4 Å from the *d* spacing between (002) planes and in case of COF-4, the *d*-spacing between (201) reflection planes was 3.3 Å. To analyse the structures of the COFs and to calculate the parameters of the unit cell, geometrical optimizations and structural models were employed using Material Studio software 8.0. The experimental patterns of COF-3 matched well with the simulated staggered AB stacking model corresponding to the tetragonal lattice with space group P4222. Also, the experimental diffraction patterns of COF-4 matched well with simulated eclipsed AA stacking model corresponding to hexagonal lattice with space group P6/m. The lattice parameters of the unit cell

were refined using Pawley refinement tool which gave the values for COF-3 as $a = b = 3.13$ Å, $c = 6.81$ Å, $\alpha = \beta = \gamma = 90°$ with $R_{wp} = 6.09\%$ and $R_p = 4.84\%$ for COF-3. Similarly, COF-4, exhibited the parameters as $a = b = 22.91$ Å, $c = 3.34$ Å, $\alpha = \beta = 90°$, $\gamma = 120°$ with $R_{wp} = 5.27\%$ and $R_p = 4.16\%$ for COF-4. (Figs. 3 & 4).

The surface areas of the COFs were further determined by nitrogen adsorption-desorption studies. Based on the nitrogen sorption isotherms, COF-3 and COF-4 were estimated to have Brunauer- Emmett-Teller (BET) surface areas of 57.9 and 133.9 m^2/g, respectively as shown in Fig. 5. From isotherm curves, both the COFs were found to show type-III adsorption. Pore calculations were performed using Barrett-Joyner-Halenda (BJH) plots. The pore sizes for COF-3 and COF-4 were calculated to be 1.9 nm and 1.5 nm respectively and the pore volumes were 0.305 cc/g and 0.937 cc/g.

FE-Scanning electron microscopy (FE-SEM) images revealed coral like morphology for both the COFs in the microscopic range and pores could be seen on magnifying the images to the nano scale range. However, COF-4 seems visibly more porous than COF-3 (Fig. 6).

HR-TEM analysis of COF-3 and COF-4 also revealed the porosity in the frameworks with the stacking between the COF-sheets (Fig. S6).

Thermogravimetric analysis (TGA) of COFs determined the thermal stabilities of both the frameworks from 30°C to 600°C. COF-3 was thermally stable up to 210°C with ~ 10% weight loss in the beginning up to 75°C plausibly because of the guest solvent molecules within the pores of the frameworks. After 210°C, there was gradual weight loss up to 440°C followed by sharp loss up to (Fig. S7). COF-4 also showed 18% loss of the weight at 70°C plausibly due to the guest solvent molecules and then, thermal stability up to 280°C, a gradual weight loss up to 400°C followed by a sharp weight loss (Fig. S7).

XPS analysis of COF-3 revealed the binding energies at 532.2 eV, 398.6 eV and 164.1 eV corresponding to the O_{1S}, N_{1S} and S_{2p} orbitals related to carbonyl, C-N and C-S bonds. In case of COF-4, the binding energies corresponding to carbonyl group and C-N bond were present suggesting the formation of enamine linkage within the frameworks. (Fig. S8)

Iodine Adsorption Studies

Adsorption of iodine vapor

Adsorption of iodine vapors was studied by exposing an appropriate amount of COF (40 mg) in a closed vessel to the iodine vapors at 77°C and ambient pressure to have the close scenario of typical nuclear fuel reprocessing conditions. During adsorption process, the deepening of the COF color from light brown to dark brown affirmed the diffusion of iodine into pores of the frameworks. COF-3 after adsorbing iodine was referred as I_2@COF-3. The iodine uptake capacity reached 0.725 g g^{-1} after 23 hours and reached the equilibrium value 1.075 g g^{-1} after three days (Fig. 7; Table 1).

Table 1
Parameters and iodine capacity of BT-COF.

COF	Pore topology	Pore size (nm)	BET surface area (m^2g^{-1})	Pore volume (cm^3g^{-1})	Theoretical capacity ($g\ g^{-1}$)	Experimental capacity ($g\ g^{-1}$)	Pore accessibility (%)
BT-COF	Tetragonal	1.9	57.9	0.305	1.51	1.08	71.5

Iodine adsorption from solution

The adsorption of iodine from *n*-hexane solution was performed at various concentrations *viz.* 50, 100, 150, 200, 250 mg L^{-1} under ambient temperature and pressure conditions. The UV-Vis spectrum of iodine solution after adsorption at various intervals of time is shown in Fig. 8 for 250 mg L^{-1} concentration. Adsorption of the iodine solution with 250 mg L^{-1} concentration increased significantly in the first one hour and then it reached the equilibrium value after 270 minutes. The removal efficiencies reached 43.01% and 65.9% after 4.5 hours for COF-3 and COF-4, respectively with the initial concentration of 250 mg L^{-1}. The adsorption kinetics was studied using pseudo-first order and pseudo-second order kinetic models. The experimental data for COF-3 fitted well with both pseudo-first order (R^2 = 0.9868) and pseudo-second order (R^2 = 0.992) kinetics with R^2 values close to each other. This suggests the involvement of both physical and chemical adsorptions. The pseudo-first and pseudo second order rate constants were calculated to be 0.0134 min^{-1} and 8.9 x 10^{-6} min^{-1} for COF-3. However, the equilibrium adsorption capacities calculated from both the kinetics curves are compared with the experimental capacity, pseudo-first order curve fitted comparable to pseudo-second order curve. In case of COF-4, pseudo-first order kinetics (R^2 = 0.9337) fitted well with the experimental data than the pseudo-second order (R^2 = 0.8747) kinetics. This pointed towards the physical interaction between iodine molecules and the frameworks of COF-4. The calculated pseudo first and second order rate constants were calculated to be 0.0054 min^{-1} and 5.1 x 10^{-5} min^{-1}(Fig. 9; Table 2).

Further, adsorption isotherms were evaluated using Langmuir and Freundlich isotherm models. Both Langmuir and Freundlich models fitted well the sorption curves, with a closely related correlation coefficient (R^2) of 0.9976 and 0.9899, respectively for COF-3 suggesting the formation of multilayer during the adsorption of iodine. The calculated Langmuir adsorption constant (K_F) was 0.0026 and maximum adsorption capacity from Langmuir model came out to be 135.1 mg g^{-1}. Also, Freundlich constant (K_L) value came out to be 10.42 and n value to be 2.06. The adsorption isotherms of the COF-4 fitted well with the Freundlich model with the correlation coefficient (R^2) of 0.9771. The Freundlich constant (K_F) and n value came out to be1.68 and 1.04, respectively. Langmuir adsorption isotherm did not fit well with the sorption curve as the calculated maximum adsorption (555.5 mg g^{-1}) was much higher than the experimental value (143.0 mg g^{-1}) although correlation coefficient (R^2) value (0.9817)

was closer to that for COF-3. This suggested that multilayer adsorption dominated over monolayer adsorption (Fig. 10; Table 3).

Table 2
Kinetic parameters for the iodine vapor adsorption on COFs.

COFs	BET surface area ($m^2 g^{-1}$)	Conc. of solution (ppm)	Experimental q_e ($mg\ g^{-1}$)	Pseudo first order			Pseudo second order		
				K_1 (min^{-1})	q_e ($mg\ g^{-1}$)	R^2	K_2 (min^{-1})	q_e ($mg\ g^{-1}$)	R^2
COF-3	57.9	250	109.0	0.0134	109.5	0.9868	8.9×10^{-6}	140.9	0.992
COF-4	133.9	250	149.5	0.0054	132.1	0.9337	5.1×10^{-5}	188.7	0.875

Table 3
Adsorption isotherm parameters for Iodine adsorption from *n*-hexane solution

COF	q_m(exp) ($mg\ g^{-1}$)	Langmuir			Freundlich		
		K_L	q_m ($mg\ g^{-1}$)	R_L^2	K_F	n	R_F^2
COF-3	109.0	0.0026	135.1	0.9976	10.42	2.06	0.9899
COF-4	149.5	0.003	555.5	0.9817	1.68	1.04	0.9771

The mechanism of the iodine adsorption was preliminarily studied by Infrared spectroscopy. It was found that the characteristic peak positions of the frameworks changed significantly before and after the adsorption suggesting the charge transfer interactions between COF structures and the iodine molecules. There were shifts in the bands of C = O, C-N from 1586 cm^{-1} to 1574 $cm^{-1}$and 1228 – 1220 cm^{-1} in case of COF-3 and from 1579 cm^{-1} to 1569 cm^{-1},1251 to 1239 in case of COF-4. This shift in the bands suggested that adsorption of iodine molecules occurred at the enamine linkages (Fig. 11). Also, adsorption of iodine within the frameworks was supported by the FE-SEM a (Fig. 12). Both the pristine COFs showed nanowire like morphology with visible porosity. The observed porosities in case of the pristine COFs were reduced upon exposure to iodine molecules suggesting the adsorption of iodine molecules within the pores of the frameworks resulting into the reduced porosity of the frameworks.

Study of Absorbed Iodine Chemical State

The detailed atomic structure and chemical valence state of iodine species in the iodine adsorbed COFs were ascertained by X-ray Photoelectron Spectroscopy (XPS). On comparing the spectra of pristine COFs and iodine adsorbed COFs, two split peaks were observed at binding energies of 630.08 eV and 619.08 eV

corresponding to the I 3d3/2 and I 3d5/2 orbitals of the iodine molecules, respectively. This suggested that iodine molecules were captured within the frameworks. Further, I_3^- showed one peak at the binding energies of 620.8 eV in-case of COF-3 suggesting the chemical interaction of heteroatoms of the frameworks with the iodine molecules (Figs. 13 & 14). This was supported by kinetic study as well where both physical and chemical adsorptions were observed. However, presence of I_3^- within the frameworks of COF-4 was not observed upon the deconvolution of I 3d peaks in the XPS spectrum. This supported only the physical adsorption of molecular iodine in case of COF-4 as also indicated by the kinetic studies.

Iodine Release Studies

Further, the release of iodine was studied by submerging the COFs in organic solvents. The color of methanol progressively changed from colorless to dark brown after the iodine-loaded samples of COF-3 and COF-4 were submerged in it at 25°C showing that the iodine was slowly coming out from the material's pore. The release of iodine was measured using UV-Vis spectroscopy (Fig. 15). Iodine signals at 290 and 359 nm demonstrated that the amount of iodine emitted by COF-3 normally increased and achieved a dynamic equilibrium in less than 60 minutes. However, with COF-4, this release was relatively slower reached the dynamic equilibrium after 180 minutes.

Conclusion

In summary, a benzothiazole-derived COF (COF-3) was synthesized by the solvothermal method and the iodine adsorption was studied in both the vapor and solution phases. To assess the effect of heteroarene scaffolds on the iodine adsorption, a previously reported phenylene diamine-derived COF (COF-4) was also synthesized under the same conditions and studied for iodine adsorption in solution phase. Both the COFs showed iodine adsorption in *n*-hexane solution with efficiencies of 109.0 mg g^{-1} and 149.5 mg g^{-1} for COF-3 and COF-4, respectively. COF-3 was also analyzed for the iodine adsorption in vapor phase and exhibited adsorption capacity of 1.07 g g^{-1}. The structures of frameworks for COF-3 and COF-4 were optimized to be tetragonal and hexagonal, respectively, with pore diameters 1.9 nm and 1.5 nm; and BET surface areas 57.9 m^2 g^{-1} and 133.9 m^2 g^{-1}, respectively. The lower iodide adsorption capacity of COF-3 as compared to COF-4 could plausibly be due to the relatively smaller surface area owing to a different framework structure and the pore topology. The smaller pore volume and BET surface area values of COF-3 result into less interaction of iodine molecules with the framework as in case of COF-3, only nearly 71% (calculated) of the pores were exposed to the iodine environment. Although, heteroatoms in the frameworks have been reported to enhance the iodine adsorption through both physical and chemical interactions; the BET surface area and pore topology/volume remained as the major deciding parameters for the efficient iodine adsorption in case of COF-3.

Declarations

Acknowledgments

Ms. Ritika Jaryal is thankful to Ministry of Education for providing fellowship assistantship. Authors are thankful to Dr. Hitesh Sharma (PTU Jalandhar, India) for his help with Material Studio Suite for simulations and modeling.

Authors' Contributions

Dr. Sadhika Khullar and Dr. Rakesh Kumar designed and conceptualized the research work. Ritika Jaryal carried out the experimental work and characterization of materials. All the authors compiled and finalized the manuscript.

Conflict of interest: The authors declare that they have no known competing financial interests.

Funding: RJ thanks Ministry of Education, Govt. of India for the research scholarship. Funds for this research were provided by Dr B R Ambedkar National Institute of Technology Jalandhar. No other external funding was available for this research work.

Data and code availability: The data that supports the findings of this study are available on request from the corresponding author.

Ethical approval: Not applicable.

Supplementary Information: Supplementary material is available at the journal's website.

Supplementary Information contains the ^{1}H-NMR spectra of the synthesized monomers (Fig. S1-S3), Schematic procedure for the synthesis of COF (Fig. S4), ^{13}C CP-MAS solid-state NMR spectra of COFs (Fig. S5), HR-TEM images of COFs (Fig. S6), TGA scans of COFs (Fig. S6), XPS spectra of COFs (Fig. S7).

References

1. British Petroleum Statistical Review of World Energy (2021), 70th Ed.
2. British Petroleum Statistical Review of World Energy (2022), 71st Ed.
3. K. Vellingiri, K. H. Kim, A. Pournara, and A. Deep (2018). *Prog. Mater. Sci*. **94**, 1–67. https://doi.org/10.1016/j.pmatsci.2018.01.002.
4. Z. J. Yan, Y. Yuan, Y. Y. Tian, D. Zhang, and G. S. Zhu (2015). *Angew. Chem. Int. Ed.* **54**, 12733–12737. https://doi.org/10.1002/anie.201503362.
5. Y. Li, Y. Li, Q. Zhao, L. Li, R. Chen, and C. He (2019). *Cellulose.* **27**, 1517-1529. https://doi.org/10.1007/s10570-019-02877-0.
6. S. Xu, S. P. Freeman, X. Hou, A. Watanabe, K. Yamaguchi, and L. Zhang (2013). *Environ. Sci. Technol*. **47**, 10851-10859. https://doi.org/10.1021/es401527q.

7. S. U. Nandanwar, K. Coldsnow, V. Utgikar, P. Sabharwall, and D. E. Aston (2016). *Chem. Eng. J.* **306**, 369–381. https://doi.org/10.1016/j.cej.2016.07.073.
8. K. Munakata, S. Kanjo, S. Yamatsuki, A. Koga, and D. Ianovski (2003). *J. Nucl. Sci. Technol*. **40**, 695–697.
9. K. W. Chapman, P. J. Chupas, and T. M. Nenoff (2010). *J. Am. Chem. Soc.* **132**, 8897–8899. https://doi.org/10.1021/ja103110y.
10. B. J. Riley, J. D. Vienna, D. M. Strachan, J. S. McCloy, and J. L. Jerden Jr. (2016). *J. Nucl. Mater.* **470**, 307–326. https://doi.org/10.1016/j.jnucmat.2015.11.038.
11. T. H. Niu, C. C. Feng, C. Yao, W. Y. Yang, and Y. H. Xu (2020). *ACS Appl. Polym. Mater*. **3**, 354–361. https://doi.org/10.1021/acsapm.0c01136.
12. M. Xu, T. Wang, L. Zhou, and D. Hua (2020). *J. Mater. Chem. A*. **8**, 1966–1974.https://doi.org/10.1039/C9TA11446G.
13. L. He, L. Chen, X. Dong , S. Zhang , M. Zhang , X. Dai, X. Liu, P. Lin, K. Li, C. Chen, T. Pan, F. Ma, J. Chen, M. Yuan, Y. Zhang, L. Chen, R. Zhou, Y. Han, Z. Chai, and S. Wang (2021). *Chem.* **7**, 699–714. https://doi.org/10.1016/j.chempr.2020.11.024.
14. P. Wang, Q. Xu, Z. Li, W. Jiang, Q. Jiang, and D. Jiang (2018). *Adv. Mater*. **30**, 1801991. https://doi.org/10.1002/adma.201801991.
15. X. Jiang, X. Cui, A. J. E. Duncan, L. Li, R. P. Hughes, R. J. Staples, E. V. Alexandrov, D. M. Proserpio, Y. Wu, and C. Ke (2019). *J. Am. Chem. Soc*. **141**, 10915–10923. https://doi.org/10.1021/jacs.9b05232.
16. T. Geng, Z. Zhu, X. Wang, H. Xia, Y. Wang, and D. Li (2018). *Sens. Actuators B Chem.* **265**, 85–91. https://doi.org/10.1016/j.snb.2017.01.005.
17. Y. Xie, T. Pan, Q. Lei, C. Chen, X. Dong, Y. Yuan, J. Shen, Y. Cai, C. Zhou, I. Pinnau, and Y. Han (2021). *Angew. Chem. Int. Ed.* **60**, 22432–22440. https://doi.org/10.1002/anie.202108522.
18. M. Wilkinson, A. Mondino, and A. Manzini (2003). *J. Radioanal. Nucl. Chem.* **256**, 413–415. https://doi.org/10.1023/A:1024583212400.
19. B. J. Riley, S. Chong, M. J. Olszta, and J. A. Peterson (2020). *ACS Appl. Mater. Interfaces*. **12**, 19682–19692. 10.1021/acsami.0c03155.
20. B. J. Riley, J. Chun, W. Um, W. C. Lepry, J. Matyas, M. J. Olszta, and X. Li (2013). *Environ. Sci. Technol*. **47**, 7540–7547. https://doi.org/10.1021/es400595z.
21. B. J. Riley , D. A. Pierce, J. Chun, J. Matyáš, W. C. Lepry, T. G. Garn, J. D. Law, and M. G. Kanatzidis (2014). *Environ. Sci. Technol.* **48**, 5832–5839. 10.1021/es405807w.
22. S. Tang, S. Choi, Y. Nan,L. L. Tavlarides (2021). *AIChE J. 67:e17137*. https://doi.org/10.1002/aic.17137.
23. Z. Yan, Y. Yuan, Y. Tian, D. Zhang, and G. Zhu (2015). *Angew. Chem. Int. Ed.* 54: 12733–12737. https://doi.org/10.1002/anie.201503362.
24. M. Janeta, W. Bury, and S. Szafert (2018). *ACS Appl. Mater. Interfaces.* **10**, 19964-19973. 10.1021/acsami.8b03023.

25. S. Park, H. An, M. B. Park, and J. Lee (2020). *Microporous Mesoporous Mater*. **294**, 109842–109847. https://doi.org/10.1016/j.micromeso.2019.109842.
26. R. Liu, W. Zhang, Y. T. Chen, Y. R. Fan, G. Z. Hu, C. Xu, Z. Han (2020). *J. Inorg. Mater.* **35**,345–351. doi: 10.15541/jim20190351.
27. J. T. Hughes, D. F. Sava, T. M. Nenoff, A. Navrotsky (2013). *J. Am. Chem. Soc.* **135**,16256–16259. doi: 10.1021/ja406081r.
28. Q. Yu, X. H. Jiang, Z. J. Cheng, Y. W. Liao, M. Duan (2021). *RSC Adv.* **11**, 30259–30269. doi: 10.1039/d1ra05223c.
29. V. V. Butova, V. A. Polyakov, E. A. Erofeeva, I. S. Yahia, H. Y. Zahran, A. F. Abd El-Rehim, A. M. Aboraia, A. V. Soldatov (2020). *Inorganica Chim. Acta.* **509**, 119678. doi: 10.1016/j.ica.2020.119678.
30. Y. R. Lee, X. H. Do, K. Y. Cho, K. Jeong, K. Y. Baek (2020). *ACS Appl. Nano Mater.* **3**,9852–9861. doi: 10.1021/acsanm.0c01914.
31. B. Valizadeh, T. N. Nguyen, B. Smit, and K. C. Stylianou (2018). *Adv. Funct. Mater.* **28**, 1801596. https://doi.org/10.1002/adfm.201801596.
32. D. Banerjee, X. Chen, S. S. Lobanov, A. M. Plonka, X. Chan, J. A. Daly, T. Kim, P. K. Thallapally, J. B. Parise (2018). *ACS Appl. Mater. Interfaces*. **10**, 10622-10626. https://doi.org/10.1021/acsami.8b02651.
33. R. Jaryal, R. Kumar, and S. Khullar (2022). *Coord. Chem. Rev.* **464**, 214542. https://doi.org/10.1016/j.ccr.2022.214542.
34. M. Chebbi, B. Azambre, C. Volkringer, and T. Loiseau (2018). *Microporous Mesoporous Mater.* **259**, 244–254. https://doi.org/10.1016/j.micromeso.2017.10.018.
35. K. W. Chapman, D. F. Sava, G. J. Halder, P. J. Chupas, and T. M. Nenoff (2011). *J. Am. Chem. Soc.* **133**, 18583–18585. https://doi.org/10.1021/ja2085096.
36. T. D. Bennett, P. J. Saines, D. A. Keen, J. C. Tan, and A. K. Cheetham (2013). *Chem. Eur. J.* **19**, 7049–7055. https://doi.org/10.1002/chem.201300216.
37. L. J. Small, R. C. Hill, J. L. Krumhansl, M. E. Schindelholz, Z. H. Y. Chen, K. W. Chapman, X. R. Zhang, S. H. Yang, M. Schroder, T. M. Nenoff, (2019). *ACS Appl. Mater. Interfaces*. **11**, 27982–27988. doi: 10.1021/acsami.9b09938.
38. K. Geng, T. He, R. Liu, S. Dalapati, K. Tian Tan, Z. Li, S. Tao, Y. Gong, Q. Jiang, and D. Jiang (2020). *Chem. Soc. Rev*. **120**, 8814–8933. https://doi.org/10.1039/C2CS35157A.
39. A. P. Côté, A. I. Benin, N. W. Ockwig, M. O'Keeffe, A. J. Matzger, O. M. Yaghi (2005). *Science*. **310**, 1166—1170. 10.1126/science.1120411.
40. T. F. Machado, M. Elisa, S. Serra, D. Murtinho, A. J. M. Valente, and M. Naushad (2021). *Polymers*. **13**, 970. 10.3390/polym13060970.
41. X. Feng, X. Ding, and D. Jiang (2012). *Chem. Soc. Rev*. **41**, 6010–6022. https://doi.org/10.1039/C2CS35157A.

42. R. Jaryal, S. Khullar, and R. Kumar (2022). *Materials Today: Proceedings.* **78**, 885-890. https://doi.org/10.1016/j.matpr.2022.12.093.
43. S. Y. Ding, and W. Wang (2013). *Chem. Soc. Rev.* **42**, 548–568. https://doi.org/10.1039/C2CS35072F.
44. J. Xiao, J. Chen, J. Liu, H. Ihara, and H. Qiu (2022). *Green Energy Environ*. https://doi.org/10.1016/j.gee.2022.05.003.
45. R. Jaryal, R. Kumar, and S. Khullar (2023). In: Shanker, U., Hussain, C.M., Rani, M. (eds) Handbook of Green and Sustainable Nanotechnology. *Springer Cham*. https://doi.org/10.1007/978-3-030-69023-6_38-1.
46. N. Huang, P. Wang, and D. Jiang (2016). *Nat. Rev. Mater*. **1**, 16068. https://doi.org/10.1038/natrevmats.2016.68.
47. Z. J. Yin, S. Q. Xu, T. G. Zhan, Q. Y. Qi, Z. Q. Wu, and X. Zhao (2017). *Chem. Comm*. **53**, 7266–7269. https://doi.org/10.1039/C7CC01045A.
48. Y. Yang, C. Tu, H. Yin, J. Liu, F. Cheng, and F. Luo (2022). *Molecules.* **27**, 9045. 10.3390/molecules27249045.
49. X. Guo, Y. Li, M. Zhang, K. Cao, Y. Tian, Y. Qi, S. Li, K. Li, X. Yu, and L. Ma (2020). *Angew. Chem. Int. Ed.* **132**, 22886–22894. https://doi.org/10.1002/anie.202010829.
50. C. Wang, Y. Wang, R. L. Ge, X. D. Song, X. Q. Xing, Q. K. Jiang, H. Lu, C. Hao, X. W. Guo, Y. A. Gao, D. L. Jiang (2018). *Chem. Eur. J.* **24**, 585–589. doi: 10.1002/chem.201705405.
51. Y. B. Zhang, L. M. Li, M. G. Wang, Z. Y. Duan (2021). *Heterocycles*. **102**, 1395–1401 doi:10.3987/COM-21-14463.
52. J. H. Zhang, J. C. Liu, Y. Z. Liu, Y. J. Wang, Q. R. Fang, S. L. Qiu (2022). *Chem. Res. Chin. Univ.***38**,456–460.doi:10.1007/s40242-022-1513-3.
53. G. J. Xu, J. H. Chang, Q. R. Fang (2020). *Chem. J. Chin. Univ.* **41**, 2667–2672. doi: 10.7503/cjcu20200624
54. Y. Li, X. G. Li, J. F. Li, W. Liu, G. E. Cheng, H. Z. Ke (2021). *Microporous Mesoporous Mater.***325**,111351.doi:10.1016/j.micromeso.2021.111351.
55. Z. L. Wen, S. L. Wang, S. Y. Fu, J. Y. Qian, Q. Q. Yan, H. J. Xu, K. M. Zuo, X. F. Su, C. Y. Zeng, Y. A. Gao (2022). *Chem. Res. Chin. Univ.* **38**, 472–477. doi: 10.1007/s40242-022-2057-2.
56. R. Chen, T. L. Hu, W. Zhang, C. Y. He, Y. Q. Li (2021). *Microporous Mesoporous Mater.* **312**, 110739. doi: 10.1016/j.micromeso.2020.110739
57. S. Song, Y. Shi, N. Liu, and F. Liu (2021). *RSC Adv.* **11**, 10512-10523. 10.1039/D0RA10587B.
58. Y. Yang, X. Xiong, Y. Fan, Z. Lai, Z. Xu, and F. Luo (2019). *J. Solid State Chem.* **279**, 120979. https://doi.org/10.1016/j.jssc.2019.120979.
59. S. H. M. Mehr, B. O. Patrick, and M. J. MacLachlan (2016). *Org. Lett.* **18**, 1840–1843. 10.1021/acs.orglett.6b00577.
60. S. Kandambeth, A. Mallick, B. Lukose, M.V. Mane, T. Heine, and R. Banerjee (2012). *J. Am. Chem. Soc.* **134**, 19524–19527. https://doi.org/10.1021/ja308278w.

Scheme 1

Scheme 1 is available in the Supplementary Files section.

Figures

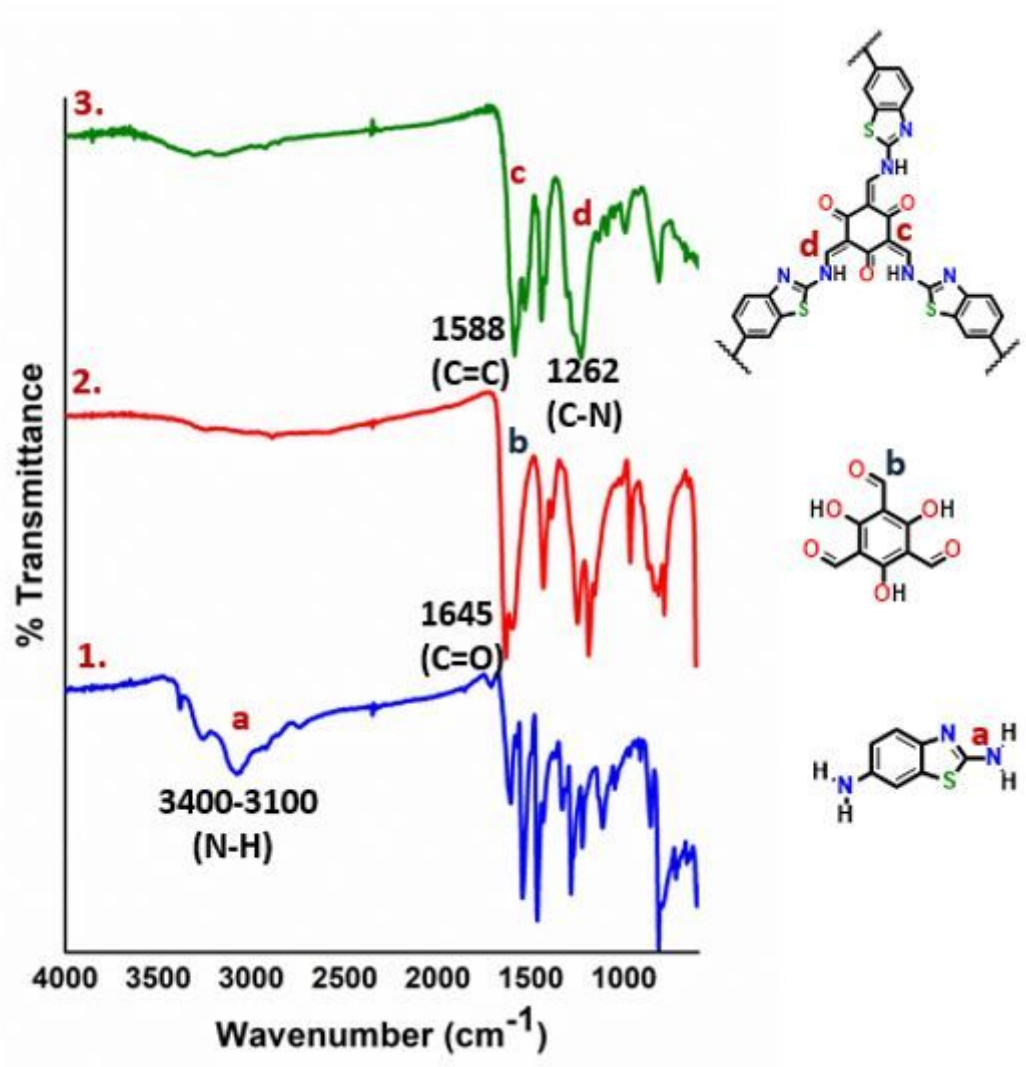

Figure 1

IR spectra of 2,6-diaminobenzothiazole (1); 2,4,6-triformylphloroglucinol (2); and COF-3 (3).

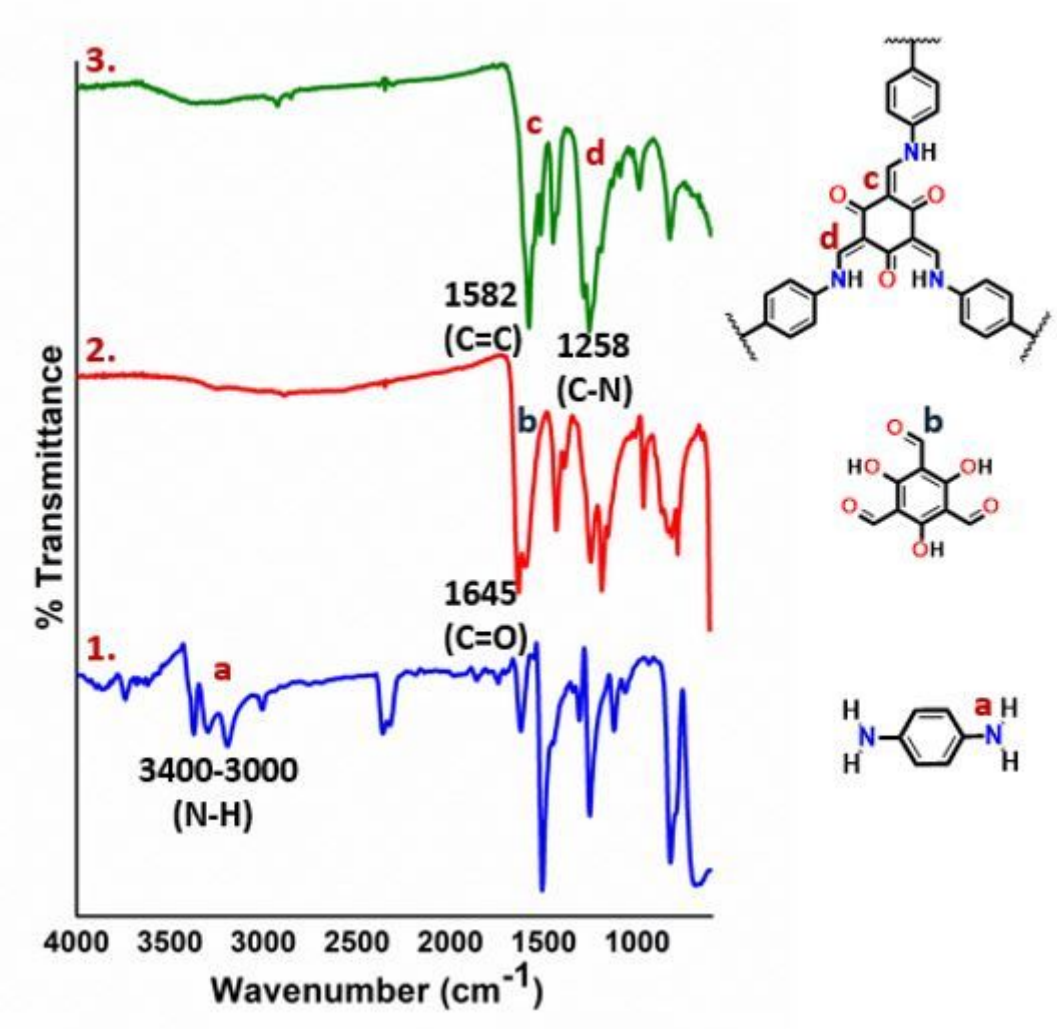

Figure 2

IR spectra of 1,4-phenylenediamine (1); 2,4,6-triformylphloroglucinol (2); and COF-4 (3).

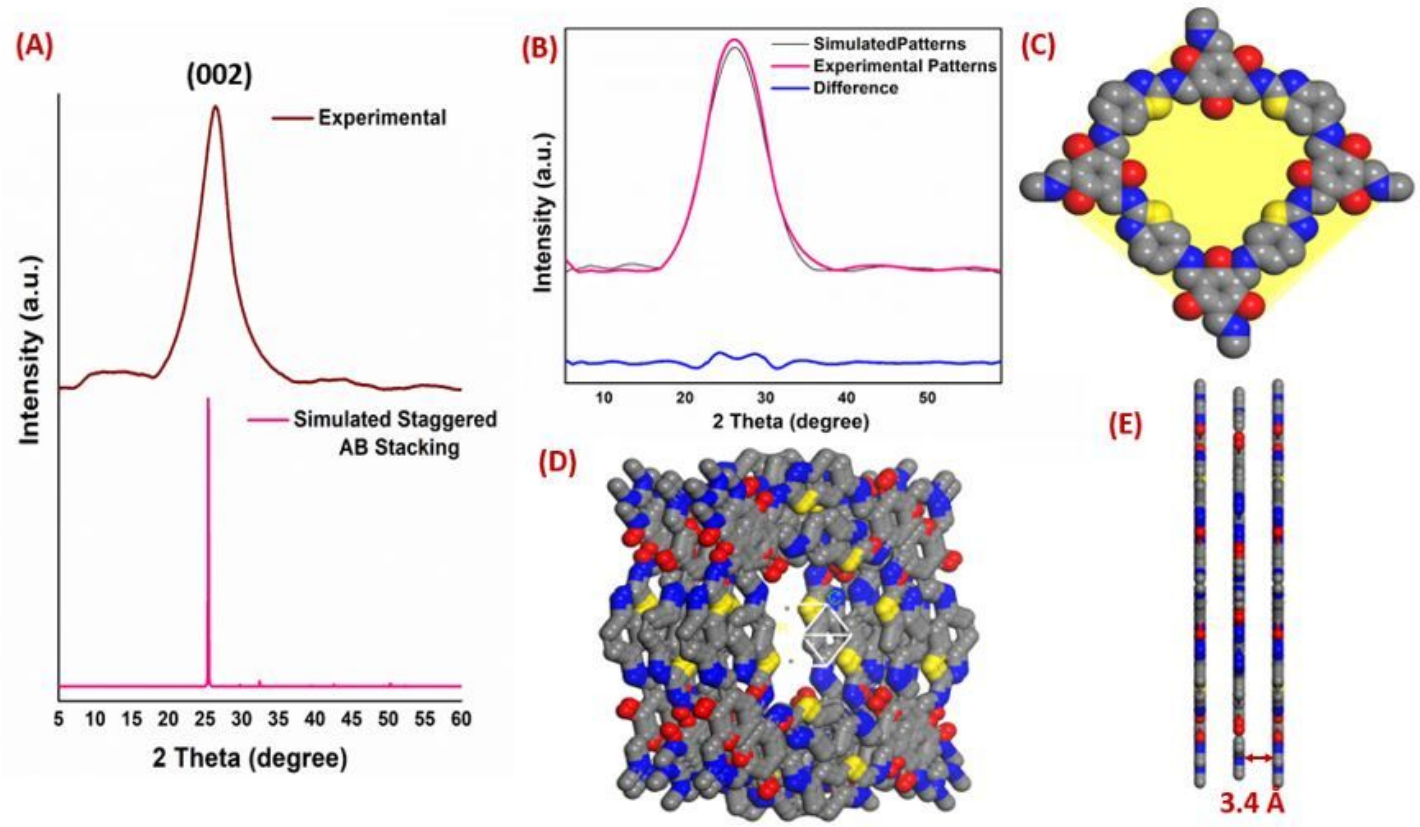

Figure 3

PXRD patterns of COF-3: observed (wine red) and simulated (pink) (A); Experimentally observed PXRD patterns (pink), simulated patterns (black) and the difference between the experimental and calculated patterns (blue) (B); Optimized tetragonal pore topology of the COF-3 (C); Reconstructed crystal structure of the COF-3 observed at orientation standard A along X, B in XY plane (D); and interplanar *d*-spacing between COF-3 layers (vertical alignment) (E).

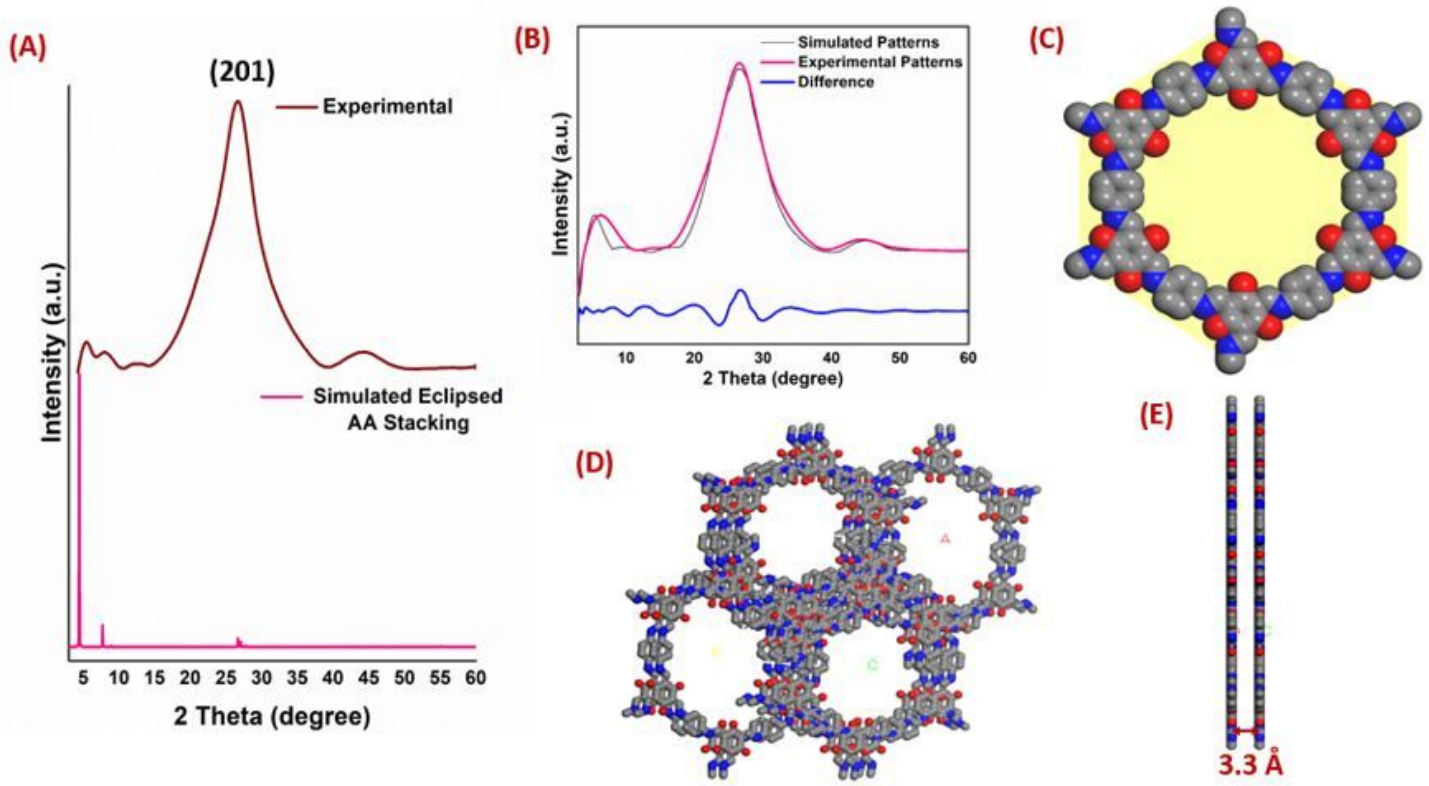

Figure 4

Comparison of the observed (wine red) and simulated (pink) PXRD patterns (A); Experimentally observed PXRD patterns (pink), Simulated patterns (black) and the difference between the experimental and calculated patterns (blue) (B); Optimized hexagonal pore topology of the COF-4 (C); Reconstructed crystal structure of the COF-4 observed at orientation standard A along X, B in XY plane (D); Interplanar *d*-spacing between the COF-4 layers (vertical alignment) (A).

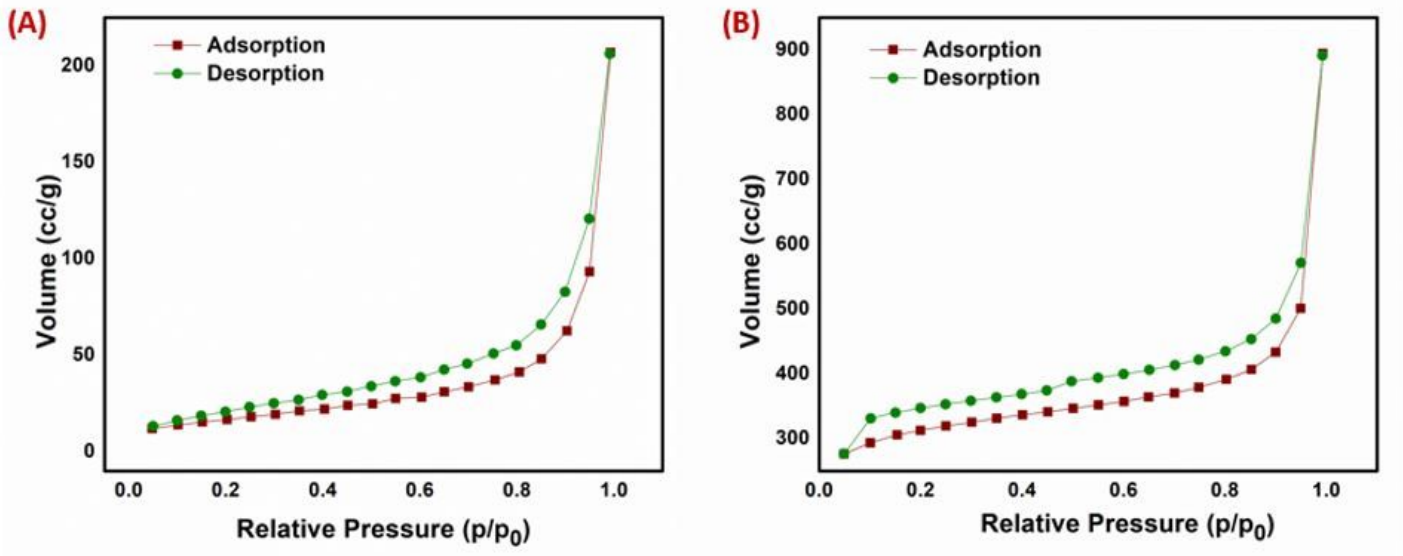

Figure 5

Nitrogen sorption isotherms of COF-3 (A) and COF-4 (B)

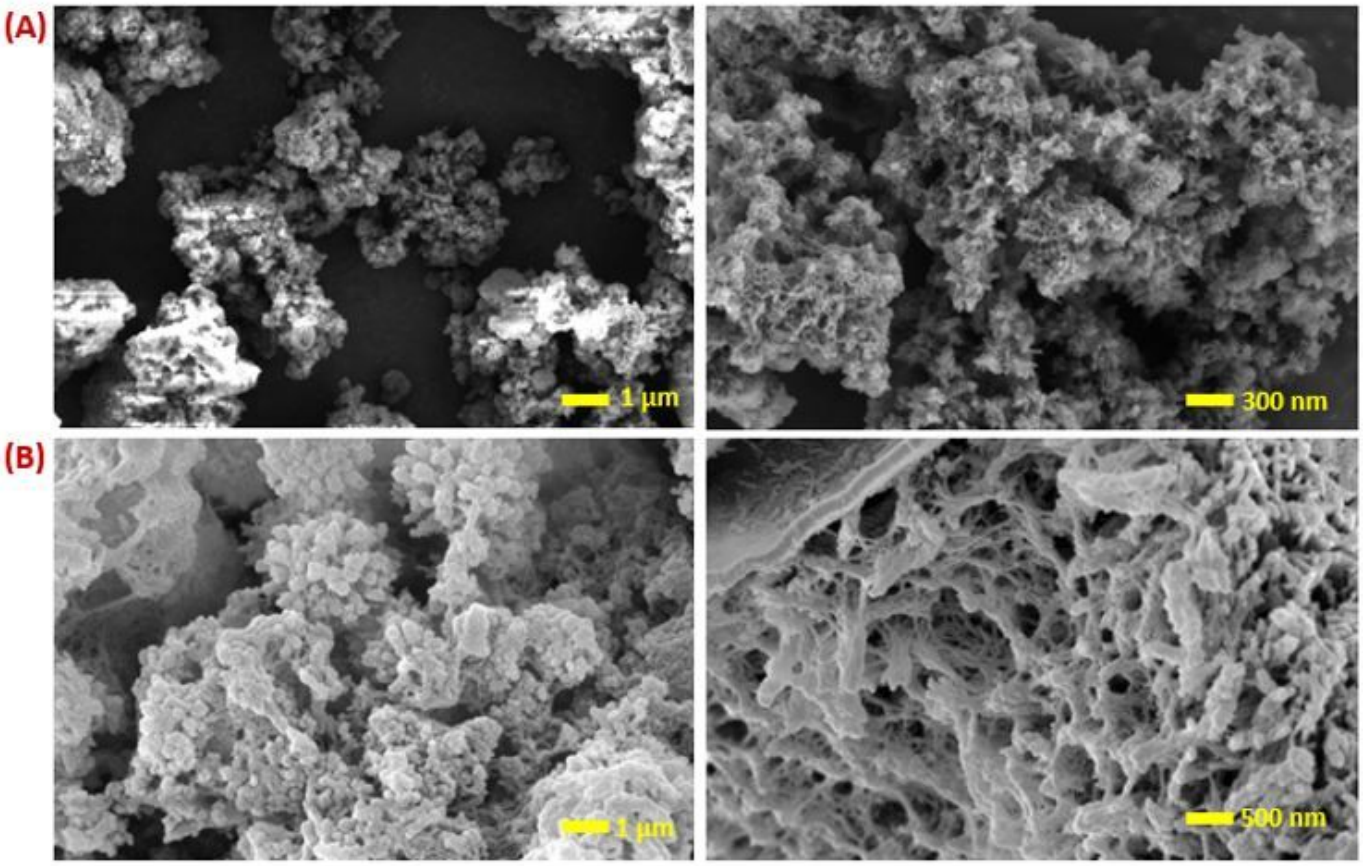

Figure 6

FE-SEM images of COF-3 (A) and COF-4 (B).

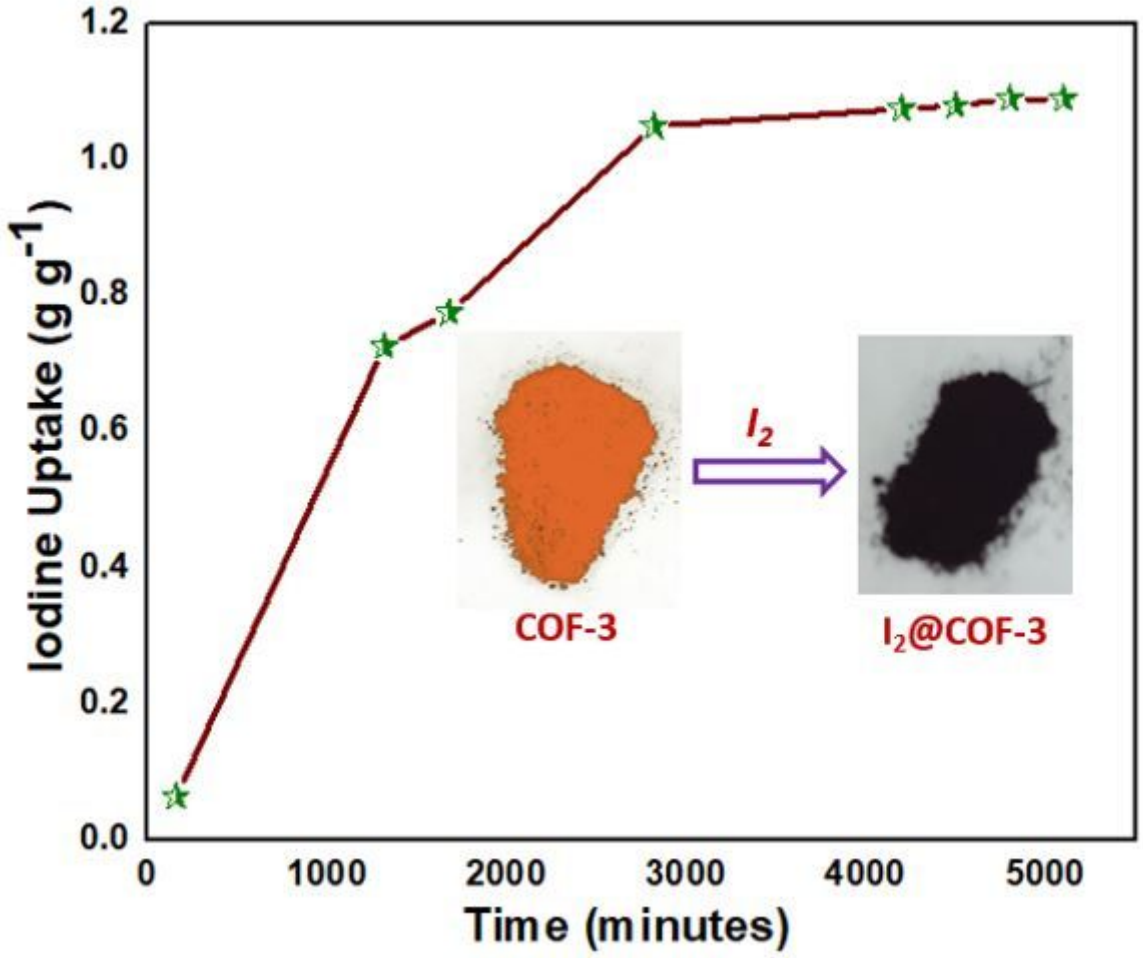

Figure 7

Adsorption of iodine vapors in COF-3.

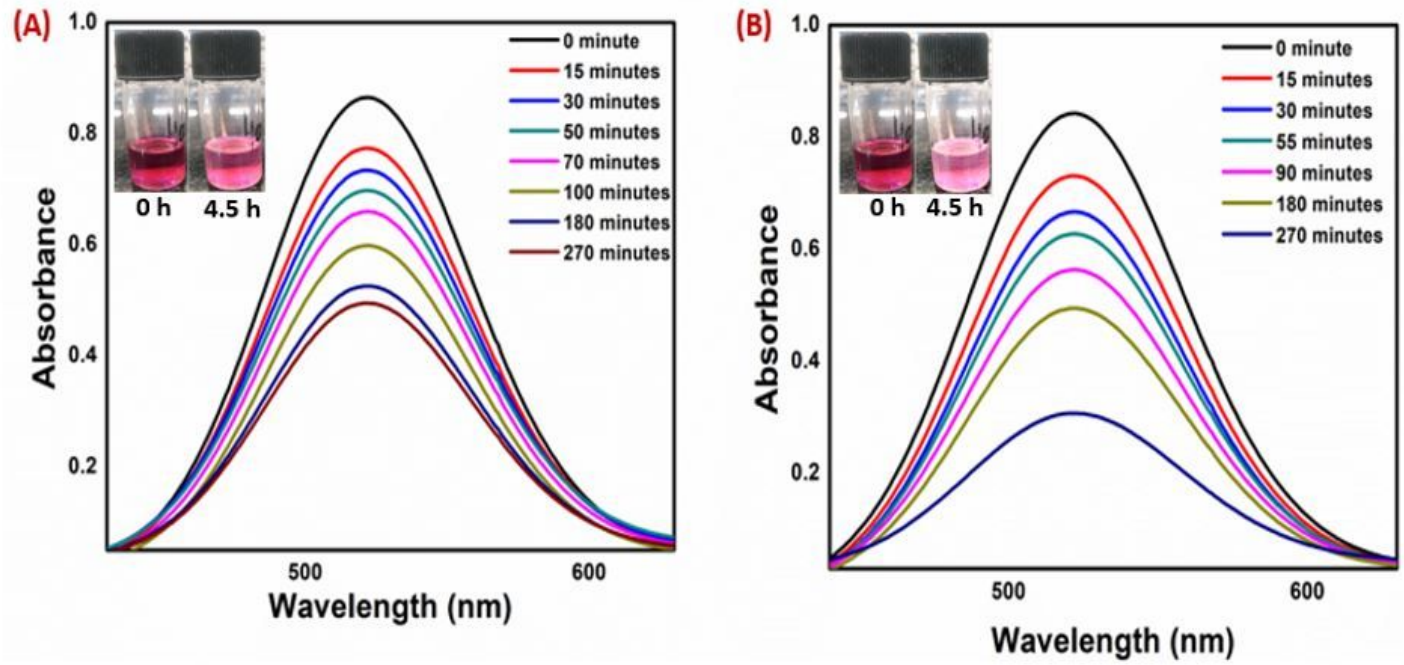

Figure 8

UV-Vis spectra for the adsorption of iodine from *n*-hexane solution with

COF-3 (A); and COF-4 (B)

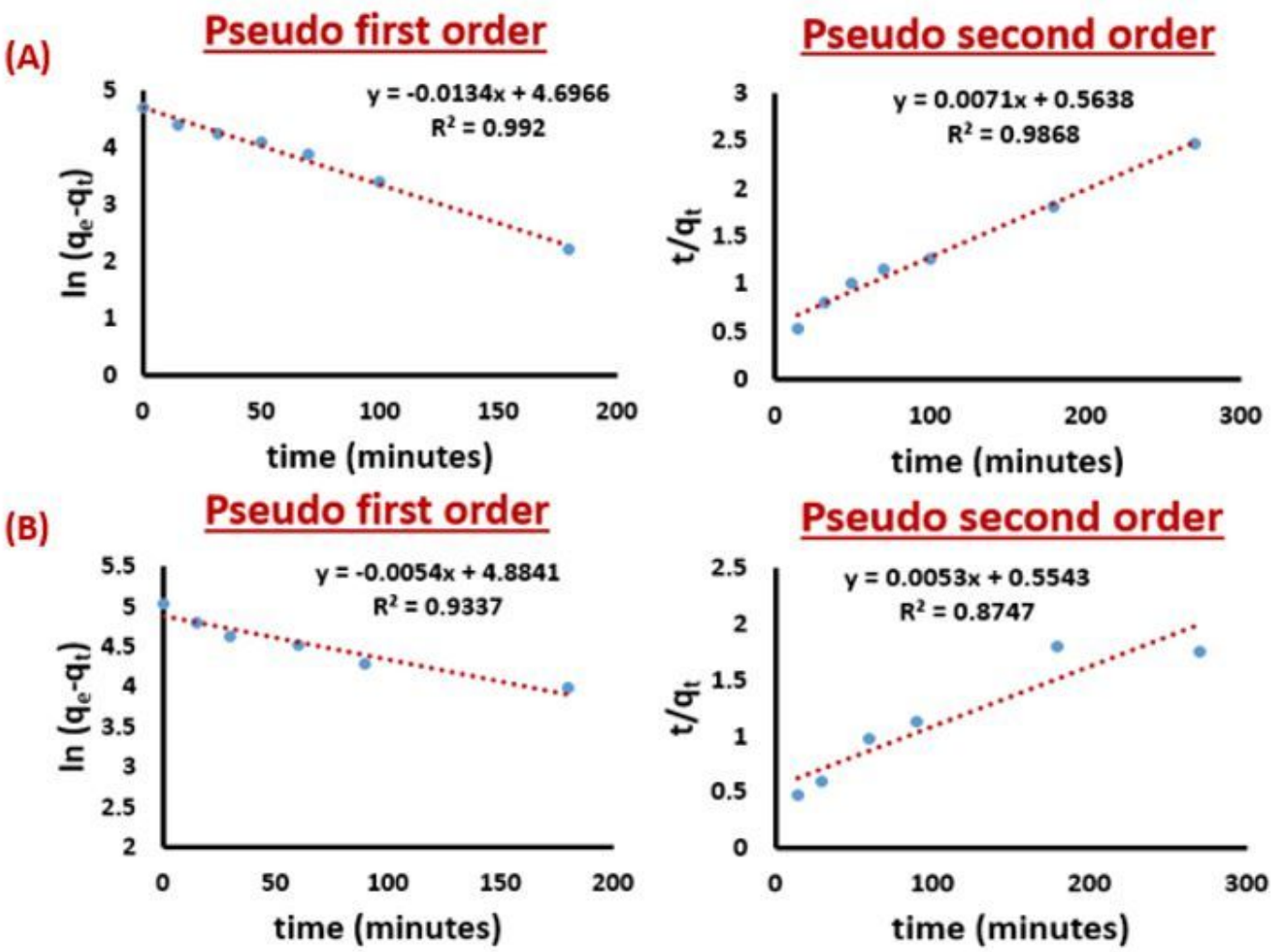

Figure 9

The fitting curves for iodine adsorption from *n*-hexane solution by COF-3 (A); and COF-4 (B).

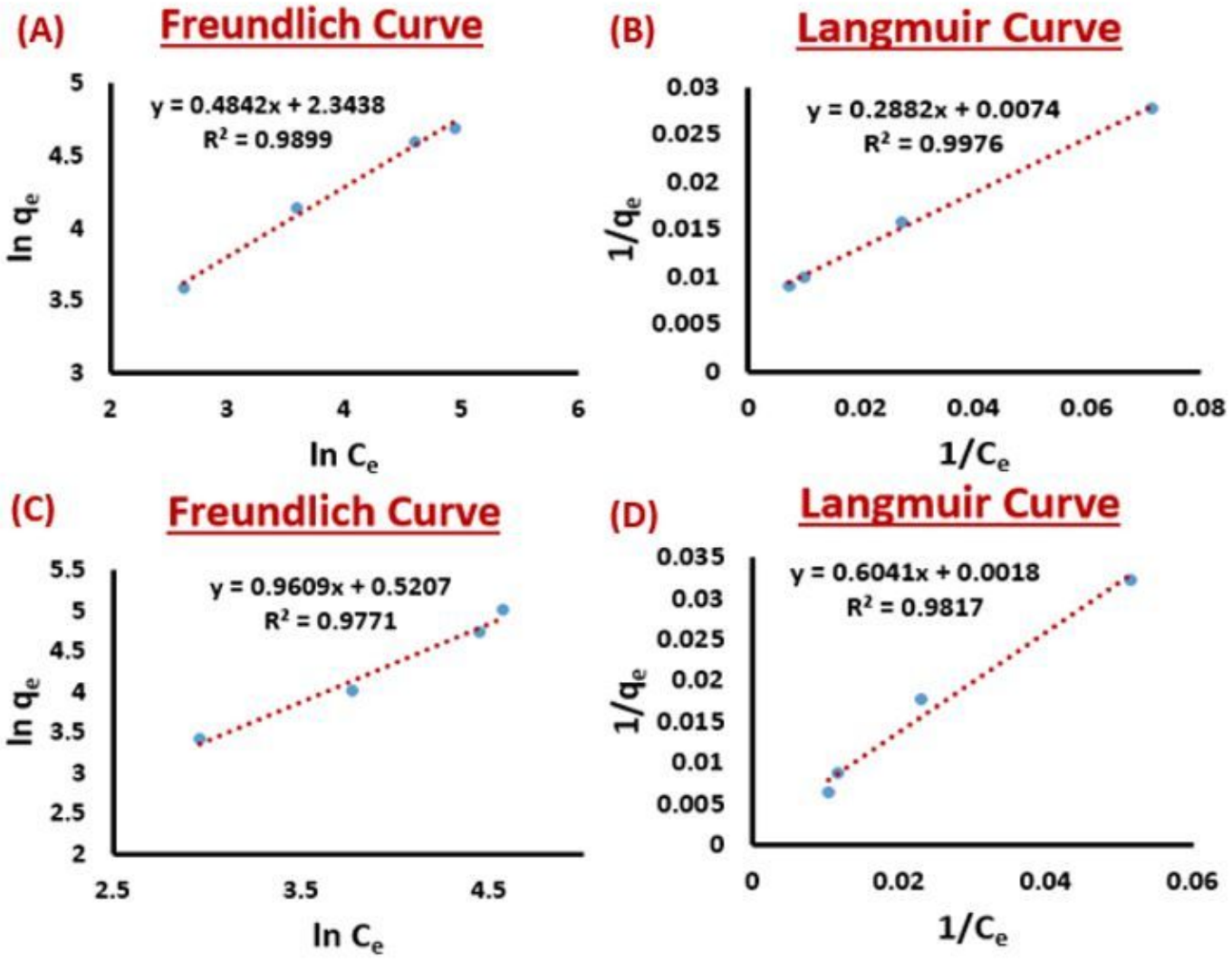

Figure 10

Freundlich fitting curves for COF-3 (A), (C); and Langmuir fitting curves for COF-4 (B), (D).

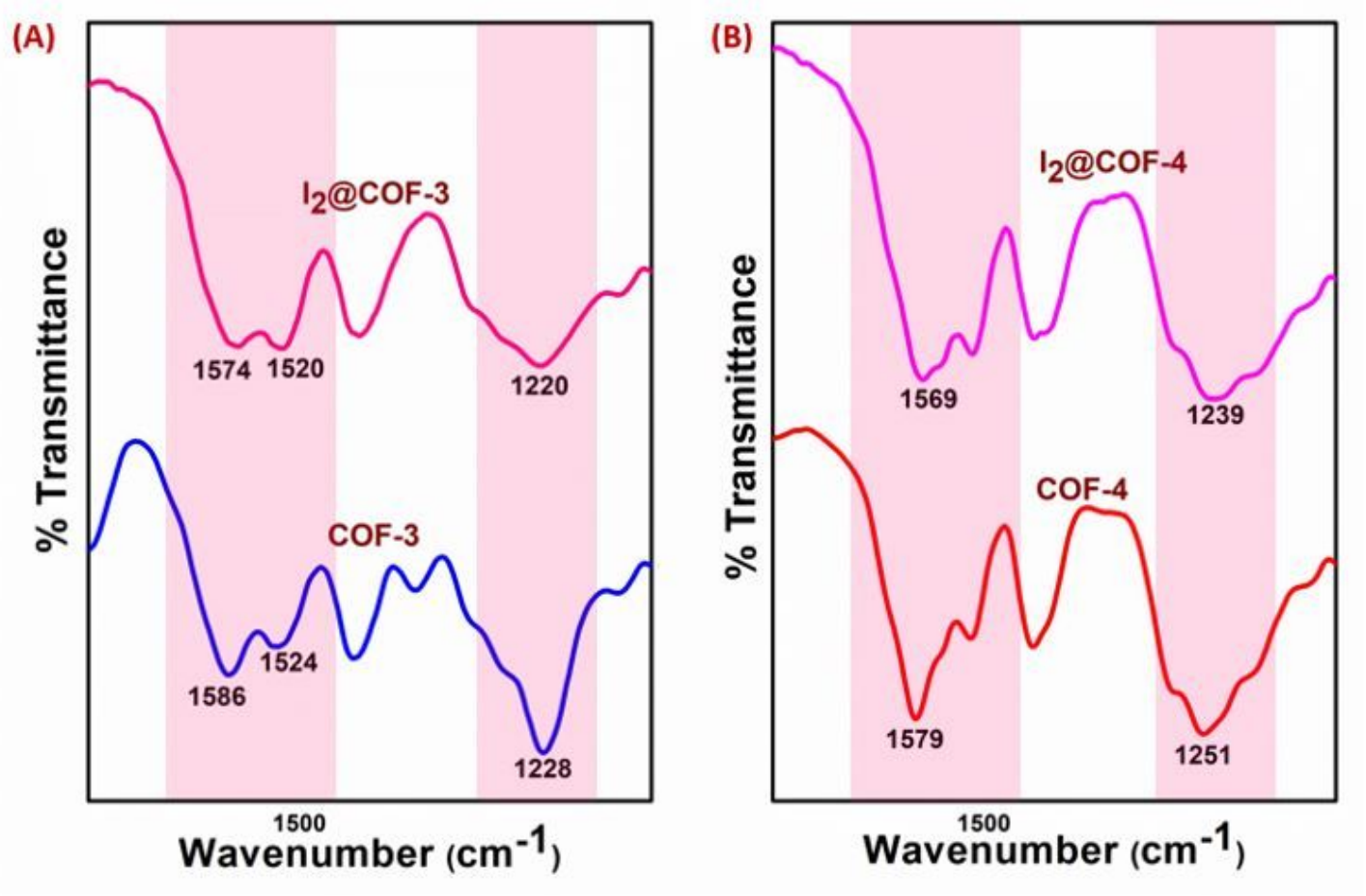

Figure 11

IR spectra of COF-3 (A); and COF-4 (B) after iodine adsorption.

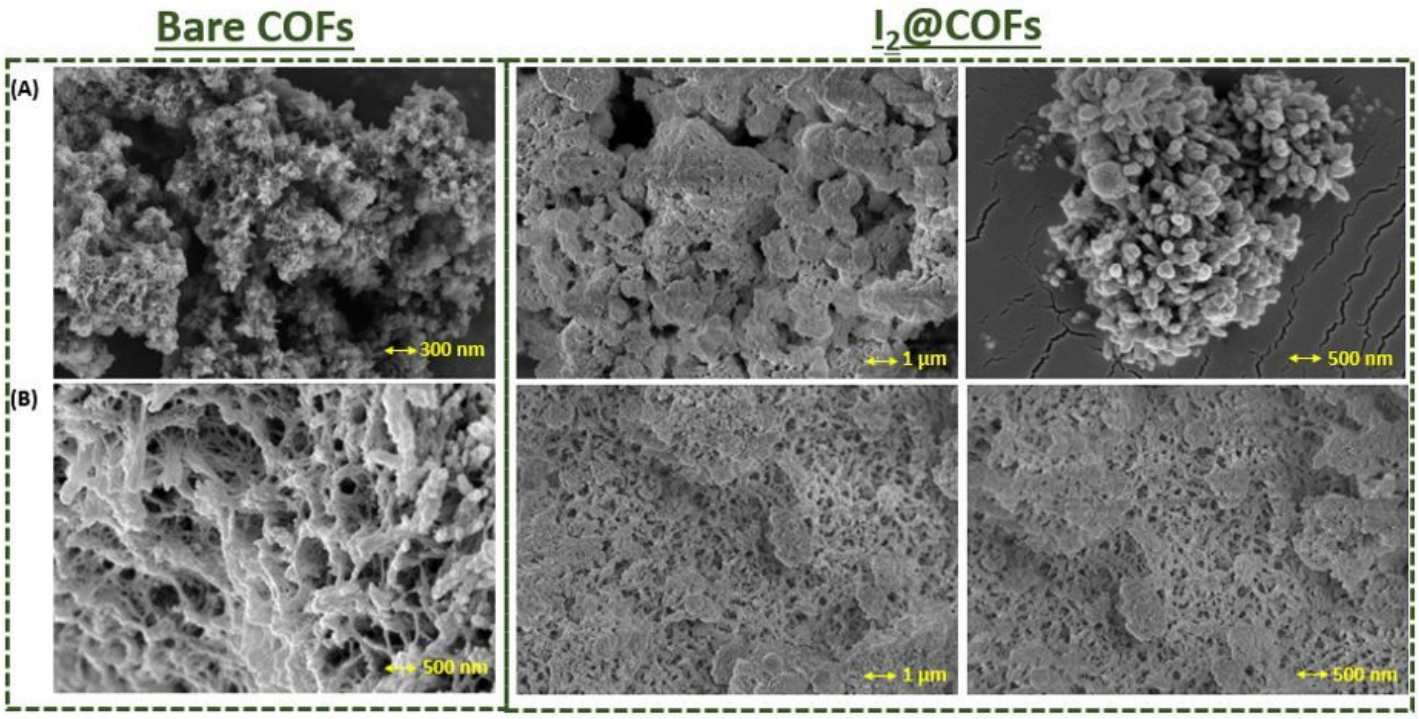

Figure 12

FE-SEM images of iodine loaded COF-3 (A); and COF-4 (B).

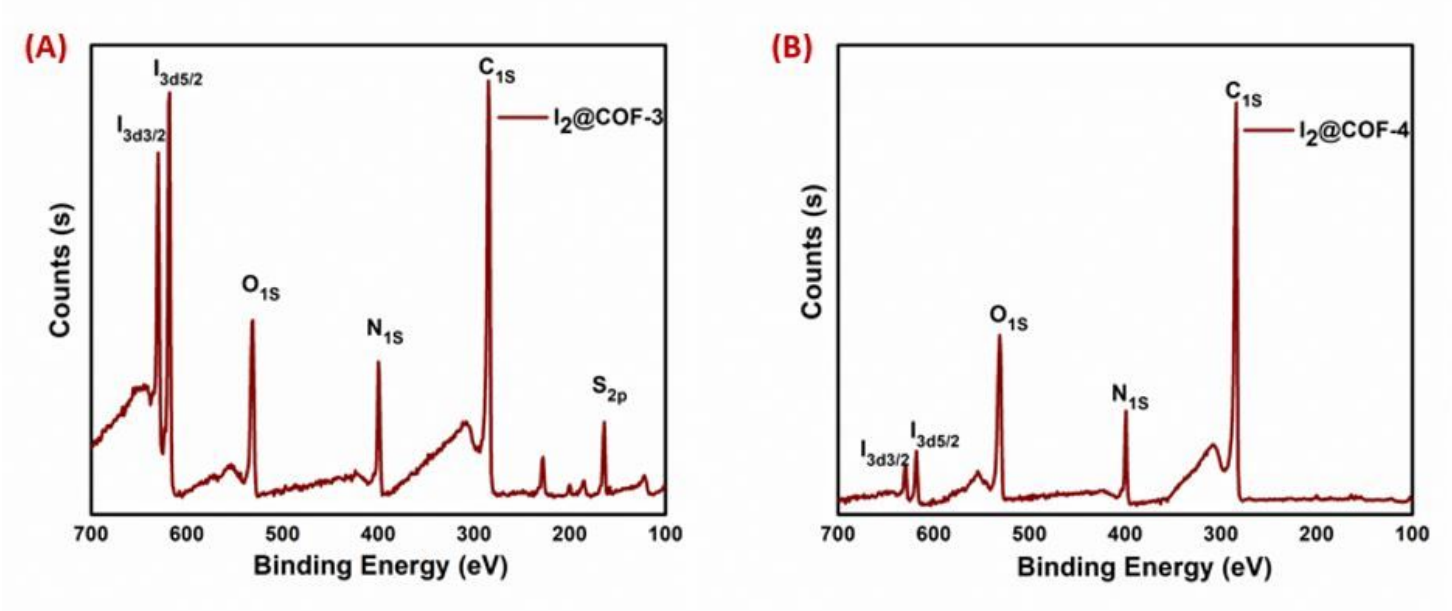

Figure 13

XPS spectra of iodine loaded COF-3(A); COF-4 (B).

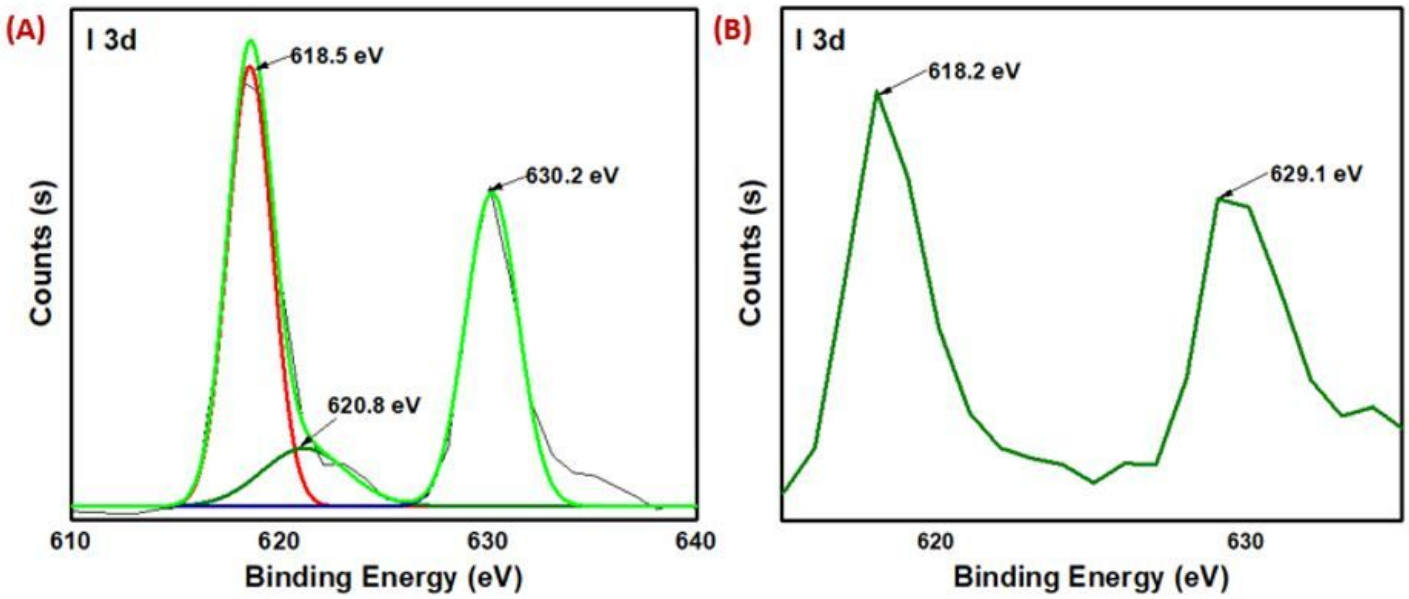

Figure 14

I3d XPS spectra of iodine loaded COF-3 (A); COF-4 (B).

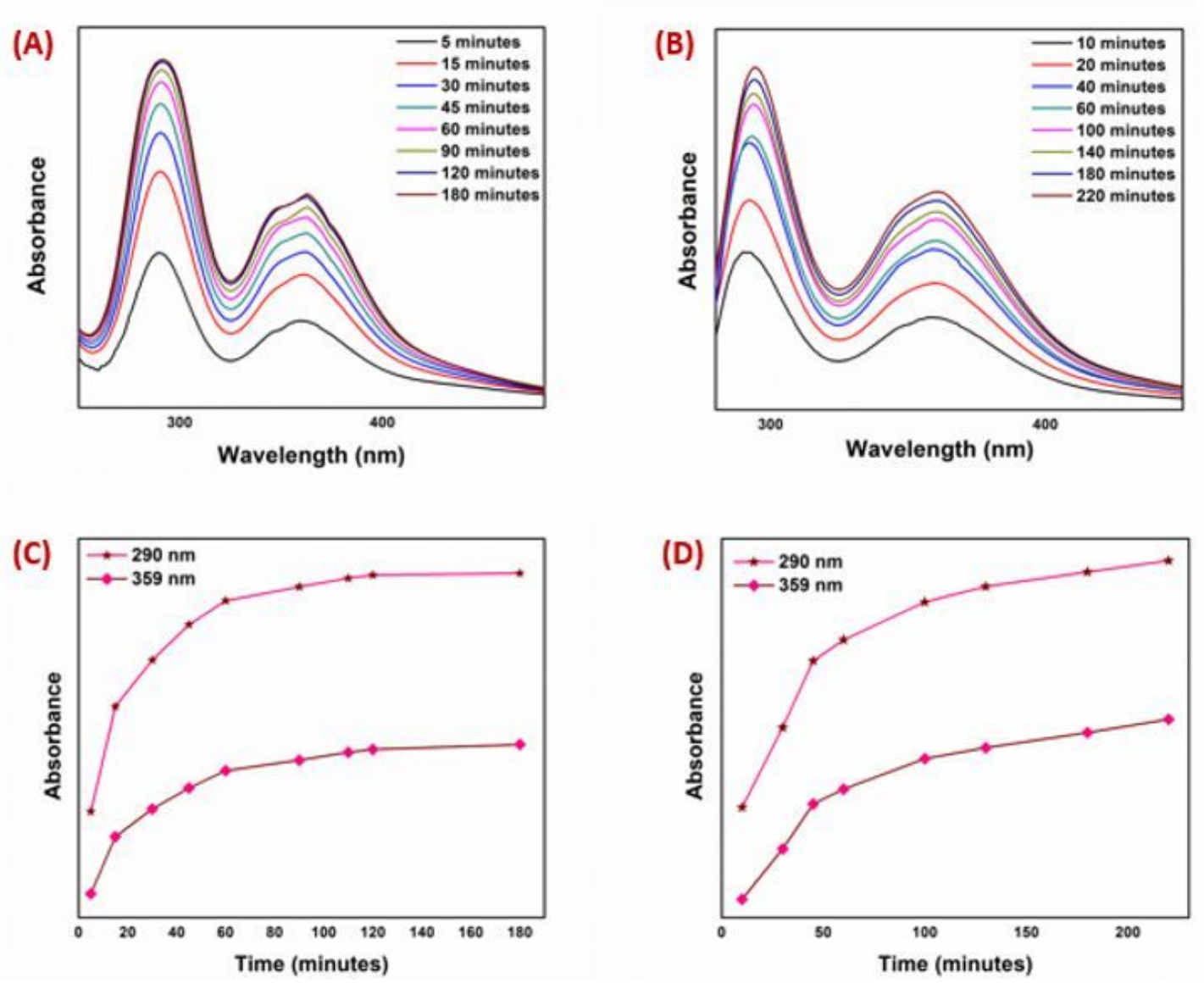

Figure 15

UV–Vis spectra for the time –dependent iodine release from COF-3 (A); and COF-4 (B); Release of Iodine from COF-3 (C); and COF-4 (D) at different times.

Supplementary Files

This is a list of supplementary files associated with this preprint. Click to download.

- SupplementaryInformationBTCOF.docx
- Graphicalabstract.jpg
- scheme1.jpg